IEEE Access
Multidisciplinary | Rapid Review | Open Access Journal

Date of publication xxxx 00, 0000, date of current version xxxx 00, 0000.

*Digital Object Identifier 10.1109/ACCESS.2020.Doi Number*

# Reduction of Ripple Toothed Torque in the Internal Permanent Magnet Electric Motor by Creating Optimal Combination of Holes in the Rotor Surface Considering Harmonic Effects

**Alireza Ramezani[1], Mohammd Ghiasi[2], (*Graduate Student Member, IEEE)*, Moslem Dehghani[2], Taher Niknam[2], (*Member, IEEE)*, Pierluigi Siano[3], (*Senior Member, IEEE),***
***Hassan Haes Alhelou[4], (Senior Member, IEEE)***

[1] Fars Regional Electrical Co, Shiraz, Iran
[2] Department of Electrical and Electronic Engineering, Shiraz University of Technology, Shiraz, Iran
[3] Department of Management & Innovation Systems, University of Salerno, 84084 Salerno, Italy
[4] Department of Electrical Power Engineering, Tishreen University, 2230 Lattakia, Syria

Corresponding authors: Hassan Hassan Alhelou (e-mail: alhelou@tishreen.edu.sy)

**ABSTRACT** Due to the widespread use of electric motors in various industries, it is very important to have optimally designed motors in that they have high efficiency and lower negative effects on the quality of the power grid. Therefore, in this paper, the effects of winding type (wide and concentrated) on ripple torque in internal permanent magnet motor (IPMM) are investigated. In order to reduce the ripple torque and to increase the average torque, by making optimal holes in the rotor surface and using the sensitivity analysis method, the structure of the IPMM is improved. In this method, the number, dimensions and location of holes are optimized using the sensitivity analysis approach, which reduces the ripple torque of the motor. Using a concentrated winding instead of a wide winding, the toothed ripple torque is reduced by approximately 75% while maintaining the average torque value. Also, by making holes in the rotor surface and optimizing them using the finite element technique and sensitivity analysis, it is demonstrated that the amount of ripple torque by 20%. In the proposed approach, it is proved that in the concentrated winding, in addition to reducing the spatial harmonics, the average amount of torque can also be improved. Obtained results of the simulation confirm the effectiveness of the proposed method.

**INDEX TERMS** Permanent Magnet Synchronous Motor, Sensitivity Analysis, Ripple Toothed Torque, Harmonic Effects

## I. INTRODUCTION

### *A. BACKGROUND*

Today, interior permanent magnet synchronous motors (IPMSMs) are largely utilized in domestic and industrial applications. This kind of electric motor, due to the type of design, has various models with different applications and noticeable efficiency. Having two useful components of reluctance and electromagnetic torque has caused these motors to have high power density. For this reason, it is suitable for use in applications that face limited volume and weight, for example in electric vehicles (EVs). The major problem faced by internal permanent magnet synchronous motors or any other electric motor is torque. Torque pulse, in addition to creating mechanical noise and differences in the quality of motor performance, causes torque fluctuations in the internal permanent magnet synchronous motor. Spatial harmonics in the magnetic field of air distance have three spatial harmonics of the field in air distance. The spatial harmonics in the magnetic field have three sources [1-3].

In terms of toothed ripple or cogging torque, several known methods were presented to reduce it in many kinds of motors that have a uniform (multilayer) axial structure [4, 5]. However, owing to differences in motor structure, these techniques cannot be used in all electric motors. For instance, the most common method for reducing cogging or toothed

This article has been accepted for publication in a future issue of this journal, but has not been fully edited. Content may change prior to final publication. Citation information: DOI 10.1109/ACCESS.2020.3041739, IEEE Access



ripple torque in transverse flux motors is to tilt or skew all armature cores with radial or axial gap topologies [6, 7].
Some kinds of toothed ring cores have also unequal distances (steps or pitch) between them, between adjacent teeth [8] or with crooked teeth [9] to suppress cogging or toothed torque.
There were also other ring cores which have segmented skew combinations [10]. Nonetheless, not all of these previous loop cores involve tilting multiple surfaces or unequal step structures to reduce a single harmonic component of a specific toothed torque. Thus, it is possible to limit the toothed torque with its low amplitude.

### B. STATEMENT OF THE PURPOSE

Due to the widespread use of internal permanent magnet (PM) motors, industry and engineers have been forced to use these motors as much as possible; one of the ways to achieve this goal is to reduce toothed ripple torque, which was useless and lowers motor efficiency [11, 12]. Methods to solve this problem have already been found, all of which are costly or have not properly reduced the desired defect, and in this study we try to find a way to reduce toothed torque that has both better efficiency and lower cost [13].
One of the basic needs of industrial societies is the use of electrical energy to produce mechanical energy required by small and large industries, and electric motors are the main converters used to convert electrical energy into mechanical energy and vice versa [14, 15].
Some recent papers focused on improving the applications of PM electric motors, for instance in the reference [16], a finite element (FE) approach for developing performance of a PM micro-motor was proposed. Authors of the paper [17] analyzed the implementation of directly photovoltaic (PV) powered DC permanent magnet motor. In addition, permanent magnet generator has been investigated in the paper [18] where used a novel industrial double stator cup rotor, and in the reference [19], the temperature and saturation changes impacts on control of PMSM were analyzed considering motor loss effects with several control approaches. In reference [20], an appropriate forecasting torque control design for 4-level open-end winding PMSM drive has been proposed. One of the common defects in magnetic motors that causes the efficiency of these motors to be low and prevents them from approaching high efficiency is the presence of a torque called toothed torque. The problem in this research is based on this approach. Accordingly, the main structure of the problem is formed and also according to the purpose of reducing this torque, a new way to solve this problem is expressed. As a result, this will increase the efficiency and effectiveness of the motor.

### C. RESEARCH PURPOSES

The practical objectives of this research are to propose a new approach to reduce the ripple toothed torque in order to provide better efficiency that lead to increase the performance of internal permanent magnet motors considering total harmonic distortion. This is done by making optimal holes in the rotor and examining its effect on reducing this torque. So this research will aim to present theoretical and mathematical approach to tackle the mentioned issues and then, providing a proposed optimal and applicable design internal permanent magnet motor. The theoretical concepts of this issue will be presented in the Section II.
In order to confirm the proposed method for selecting the desired winding, we compare the results of the proposed concentrated winding with the results of wide winding.

### D. HYPOTHESIS

In this article, hypotheses are generally divided into basic categories:
• The beginning and end parts of the rotor have the most changes compared to the middle part.
• If one part of the rotor changes superficially and the other part changes deeply, it reduces the toothed ripple torque.
• The width or concentration of the winding and the number of holes affect the ripple torque.

### E. RESEARCH INNOVATION

In this research, the causes of toothed torque in the internal permanent magnet motor are presented based on a new model in calculating and evaluating existing real problems, and if this torque exists, a solution to this problem is presented. In this regards, creating physical holes on the rotor as well as modeling and then examining and evaluating the impact of this method are the innovation of this research. Accordingly, following the reduction of the problem associated with the presence of ripple torque, this solution can be a new idea in reducing the impact of this torque as well as increasing the efficiency and functional efficiency of magnetic motors.

### F. ARTICLE STRUCTURE

In Section 2, we will make an introductory statement about permanent magnet motors as well as their design principles. In Section 3, we will model the proposed problem. Three-phase structures that can support this type of winding are then presented. Appropriate criteria for selecting the appropriate composition of the groove (stator slots) on the pole are discussed. In order to further confirm the selection of the desired winding, we use the results of the centralized winding with the results of a typical wide winding. In Section 4, the expressed models are simulated in software and then the results of the simulation are reviewed and analyzed. And finally in the Section 5, conclusions are expressed and also suggestions are made to continue the process of this research.

## II. THEORETICAL CONCEPTS

Given what has been said about the performance of the internal permanent magnet synchronous motor, the need to

This article has been accepted for publication in a future issue of this journal, but has not been fully edited. Content may change prior to final publication. Citation information: DOI 10.1109/ACCESS.2020.3041739, IEEE Access



optimize the performance of these motors becomes apparent. Determining the design parameters of a permanent magnet synchronous motor, which has torque without fluctuations, has always been of interest to experts.

### A. CLASSIFICATION OF PERMANENT MAGNET ELECTRIC MOTOR

There are various methods for classifying PMMs [21], including the orientation of the magnetic field, the position of the rotor relative to the stator, the shape of back electromotive force (BEMF), and the excitation and location of the magnet in the rotor. Depending on the position of the permanent magnet or the structure of the rotor, there are three types of permanent magnet synchronous motors in the industry:

- Surface permanent magnet motor (SPM)
- Permanent magnet electric motor with permanent surface magnetism
- Internal permanent magnet motor (IPM)

Figure 1 shows the common schematic types of induction and permanent magnet motors.

### B. PRESENTED ALGORITHM FOR DESIGN OF THE PERMANENT MAGNET ELECTRIC MOTOR

In this section, we explain how to achieve the desired parameters in electric motor design:

1- Making decision to design electric motor, depending on the application of the motor, whether it has an internal rotor or an external rotor

2- Determining the dimensions of the electric motor depending on the application

3- Selecting the most suitable stator slots' pole combination. In designing a permanent internal magnet motor, the number of poles depends on the following:

- Magnet material used and magnet strength
- Type of rotor used internally or externally
- Mechanical strength of rotor and magnets
- Rotor rotation speed
- Desired inertia

4- Selecting the thickness of the air gap. It is usually desirable to keep the air gap as small as possible.

The flowchart of the proposed motor design is shown in Figure 2. Appropriate experimental values of air distance are given in Table I [22].

TABLE I
APPROPRIATE EXPERIMENTAL VALUES OF AIR GAP

| Size of electric motor | Thickness of air gap (mm) |
|---|---|
| Small Electric Motor | 0/254 – 0/127 |
| Average Electric Motor | 0/508 – 0/381 |
| Big Electric Motor | 0/889 – 0/635 |

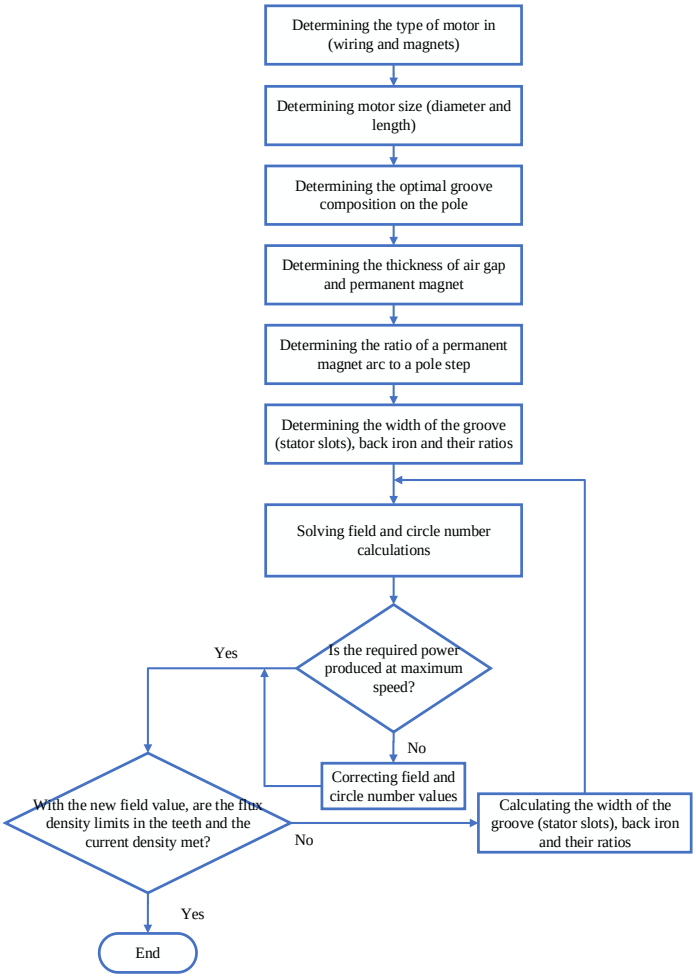


**FIGURE 2.** The flowchart of the proposed motor design

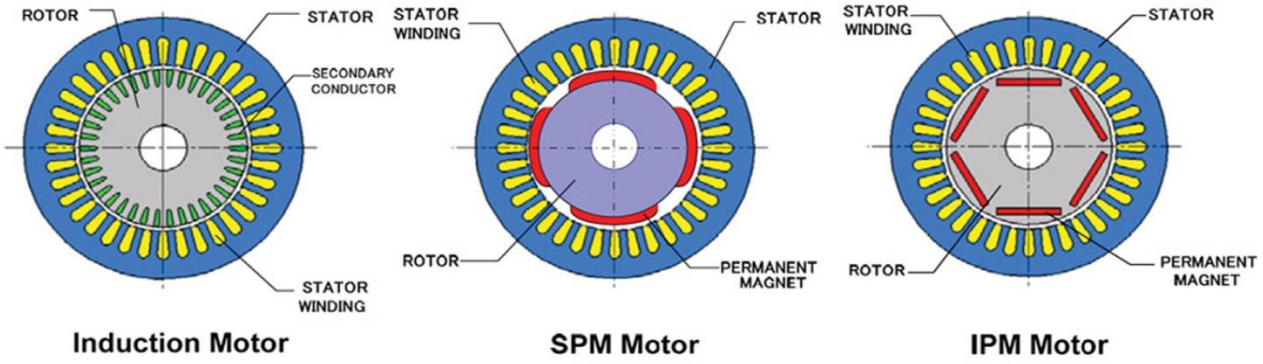


**FIGURE 1.** Common schematic types of induction and permanent magnet motors

This article has been accepted for publication in a future issue of this journal, but has not been fully edited. Content may change prior to final publication. Citation information: DOI 10.1109/ACCESS.2020.3041739, IEEE Access



5- Determining the thickness of a permanent magnet. The thickness of a permanent magnet is usually determined to reduce the risk of demagnetization. In addition, the characteristic of a permanent magnet is effective in attenuating the optimal flux. For the initial design, the thickness of a permanent magnet 5 to 10 times the thickness of the air gap is usually suitable.
6- The ratio of the permanent magnet arc to the pole step is selected so that it has the lowest possible toothed torque.
7- Determining ($\lambda_s$): the ratio of groove (stator slots) width ($w_s$) to the total groove width and tooth width ($w_t$), which is defined in equation (1). One pole step is shown in Figure 3.

$$\lambda_s = \frac{w_s}{w_s + w_t} \quad (1)$$

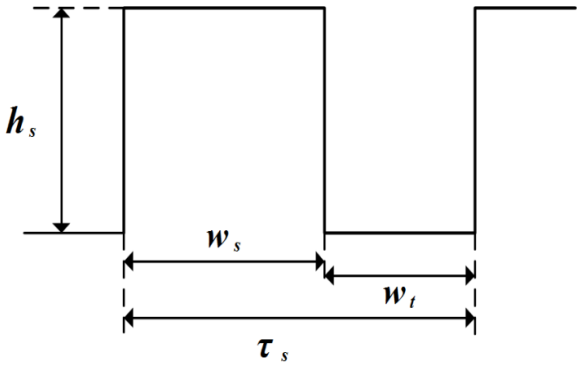


**FIGURE 3.** One pole step

8- Experimental values for ($\lambda_s$) are between 0.35 - 0.65. A value of 0.5 is selected for the initial design. We should determine ($\lambda_{hs}$) the ratio of groove (stator slots) height ($h_s$) to groove width, which is equal to:

$$\lambda_{hs} = \frac{h_s}{w_s} \quad (2)$$

The values of ($\lambda_{hs}$) are selected between 2 and 3, with the initial value of 2.5 being selected. If this ratio is high, it means that the stator slots are deepened and therefore the Back Iron is reduced and therefore it becomes saturated and the production torque is reduced. Also, the inductance of the scattering of the groove becomes problematic. If this coefficient is small, it means that the groove is very small and the current density value exceeds the nominal value.
9- The groove opening width ($w_o$) should be selected as small as possible to reduce the toothed ripple torque.
Of course, the amount of groove opening depends on the method of placing the winding in the groove. This value can affect the scattering inductance of the groove, so it is considered as a design parameter.
10- Tooth tip is also considered because it is effective in dispersion inductance. With an approximate calculation, its value is considered equal to its width.
11- Determining the thickness of the iron behind the flux; assuming that the flux density in the air gap is equal to 0.8 Tesla. This thickness is chosen so that the maximum flux density is 1.8 Tesla.
12- Determining the value of remnant flux-density ($B_r$). Different parameters affect the appropriate selection of Br. For example: the maximum flux density in the air gap, the teeth and the iron behind the groove should not exceed the nominal value, on the other hand, in paper [22], it has been shown that the use of permanent magnets with high $B_r$ can significantly reduce the size of the inverter. If the motor terminal parameters are known, the $N_c$value of $B_r$ can be analytically obtained from the equation (3) as:

$$\psi_m = \frac{K_1 B_r N_c}{p} \quad (3)$$

Where $\psi_m$ is flux-linkage, $K_1$ is the fixed coefficient of motor and is obtained using the dimensions of the machine and the type of winding, and p is the number of pair poles. The values are selected so that the characteristic current is equal to 1 per unit and the optimal flux attenuation condition is met. At this stage, the basic design parameters are obtained. In the following, the whole motor steps are simulated and the values of these parameters are changed to estimate the constraints.
13- At this stage, the motor is simulated at maximum speed and the amount of power produced at maximum speed is obtained. If the output power is not equal to the rated output power, the value of Br changes to the required value.
14- It is checked that the electric motor gives the desired torque and power at the base speed, the amount of flux density in the teeth and air distance is checked. The grain size and yoke vary to the required value to estimate the flux density limit. The amount of current density in different applications is given in Table II [20, 23, 24].

TABLE II
CURRENT DENSITY VALUES

| Motor conditions | current density (A/mm2) |
|---|---|
| Completely covered | 1.5 - 5 |
| Outdoors or cooling with air fan | 5 - 10 |
| Equipped with coolant | 10 - 30 |

15. If the parameters change, we return to step 12 and the steps are repeated; until the restrictions and constraints are fully met.

### *C. Three-phase structures with a concentrated winding*

Three-phase electric motors with centralized winding are often limited to windings with a step of less than 120 °. These windings are less efficient than the number of slots-per-phase-per-pole (SPP) = 1. As the number of poles of the electric motor increases, the number of structures on which the concentrated winding can be applied increases considerably. This makes it possible to introduce an electric groove on phases smaller than one. Due to the three-phase nature of the electric motor, possible combinations of grooves on the pole that can provide a true balanced winding meet the following condition:

This article has been accepted for publication in a future issue of this journal, but has not been fully edited. Content may change prior to final publication. Citation information: DOI 10.1109/ACCESS.2020.3041739, IEEE Access



$$\frac{s}{(GCD(s,2p))} = 3c \quad (4)$$

The first parameter is the greatest common divisor (GCD), also (s) represents of the number of stator slots, and (2P) is the number of rotor poles of the electric motor; and c is a positive integer. Arrays that have higher efficiencies have less than or equal to 0.5 phase grooves on the pole. It is also possible to have three-phase arrangements with grooves on the pole on a phase larger than 1 or 2, but these makeups are not effective and have lower efficiency.

### *D. CRITERIA FOR PROPER SELECTION OF GROOVES ON THE POLE*

There are several groove-pole combinations that can support centralized windings. The parameters here are the lowest common multiple (LCM), and the number of stator slots poles and rotor poles (s, 2P) of the electric motor.

The second important parameter is the ratio of the number of grooves multiplied by the number of poles and the LCM between them, denoted by *K*.

We have it mathematically as follows:

$$K = \frac{s \times 2p}{(LCM(s.2p))} \quad (5)$$

Table III summarizes the LCM values for each of the grooves on the poles. Evaluation of the *K* parameter to select the appropriate groove composition on the pole is provide in Table IV

TABLE III
THE LCM PARAMETERS (S, 2P) TO SELECT THE APPROPRIATE GROOVE (STATOR SLOTS) COMPOSITION ON THE POLE

| s, 2p | 2 | 4 | 6 | 8 | 10 | 12 | 14 | 16 | 20 | 22 | 26 | 28 |
|---|---|---|---|---|---|---|---|---|---|---|---|---|
| 3 | 6 | 12 | 6 | 24 | 30 | 12 | 42 | 48 | 60 | 66 | 78 | 84 |
| 6 | - | 12 | 6 | 24 | 30 | 36 | 42 | 48 | 60 | 72 | 78 | 84 |
| 9 | - | - | 18 | 72 | 90 | 36 | 126 | 144 | 180 | 198 | 234 | 252 |
| 12 | - | - | - | 48 | 60 | 72 | 84 | 48 | 60 | 132 | 156 | 168 |
| 15 | - | - | - | - | 30 | 60 | 210 | 240 | 60 | 330 | 390 | 420 |
| 18 | - | - | - | - | - | 36 | 126 | 144 | 180 | 198 | 234 | 252 |
| 21 | - | - | - | - | - | - | 42 | 336 | 420 | 462 | 546 | 84 |
| 24 | - | - | - | - | - | - | - | 96 | 120 | 264 | 312 | 168 |

TABLE IV
THE *K* PARAMETERS TO SELECT THE APPROPRIATE GROOVE (STATOR SLOTS) COMPOSITION ON THE POLE

| s, 2p | 2 | 4 | 6 | 8 | 10 | 12 | 14 | 16 | 20 | 22 | 24 |
|---|---|---|---|---|---|---|---|---|---|---|---|
| 3 | 1 | 1 | - | 1 | 1 | - | 1 | 1 | 1 | 1 | - |
| 6 | 2 | 2 | - | 2 | 2 | - | 2 | 2 | 2 | 2 | - |
| 9 | - | 1 | 3 | 1 | 1 | 3 | 1 | 1 | 1 | 1 | 3 |
| 12 | 2 | 4 | - | 4 | 2 | - | 2 | 4 | 4 | 2 | - |
| 15 | - | - | - | 1 | 5 | - | 1 | 1 | 5 | 1 | - |
| 18 | - | - | 6 | 2 | 2 | 6 | 2 | 2 | 2 | 2 | 6 |
| 21 | - | - | - | 1 | 1 | - | 7 | 1 | 1 | 1 | - |
| 24 | - | 4 | - | 8 | 2 | - | 2 | 8 | 4 | 2 | - |

In order to achieve the highest average torque output, we need to calculate the effective number of stator windings that participate in torque generation, so we have to introduce a new item $k_{w1}$ which represents the effective number of turns of stator windings that participate in the production of torque. The maximum $k_{w1}$ is selected to achieve the highest average output torque. The reason for this is in the following as [25]:

$$T = \frac{1}{4\pi} k_{w1} n_1 n_t S B_{gmax} A_g I_{max} \cos(\gamma) \quad (6)$$

Where $n_1$ represents the number of layers per groove, $n_t$ is the number of revolutions of a tooth, S defines the number of grooves, $B_{gmax}$ denotes maximum value of airflow flux density during pregnancy, $A_g$ represents the air gap level, $I_{max}$ provides the maximum phase current and γ is the angle between the direction of the stator current vector and the q axis, which is perpendicular to the rotor of the rotor of the permanent magnet (in electrical degrees).

According to this relation, If $k_{w1}$ is low, they participate to produce torque. If $k_{w1}$ is low, to produce the same torque, either the number of revolutions should be increased or the current needs to be increased, which in total increases the copper losses. The term synchronous component is used to emphasize that this coefficient refers to a component of the spatial winding function (for example *m.m.f.* distribution) that participates in the production of torque, and lower-degree harmonics play no role in the production of average torque.

2- The choice of the highest LCM, the reason for this choice is that the smallest common coefficient of 2p and s represents the number of cogging torque pulses (N) in a complete mechanical rotation [26] which:

$$N = LCM(s, 2p) \quad (7)$$

Since the higher cogging torque typically follows lower amplitude of this torque, the highest possible value for N should be chosen.

3- Choosing a makeup with high values of *K* [27], the value of *K* is important, because it expresses the degree of symmetry of the electric motor. In fact, *K* represents the sum of radial forces. If the value of *K* is one or any individual number, it means that the radial forces have high values. Also, the symmetry of the excitation current of the windings reduces or eliminates these radial forces.

4- Depending on the nature of the application that the PM motor can have, there is a good reason to use a single-layer winding; certain combinations of grooves on the pole can support the single-layer winding. Therefore, this should be considered in selecting the groove on the pole on the phase.

According to the above points, we can choose the right combination of groove-pole.

This article has been accepted for publication in a future issue of this journal, but has not been fully edited. Content may change prior to final publication. Citation information: DOI 10.1109/ACCESS.2020.3041739, IEEE Access



### E. Determining the arrangement of the concentrated winding on the groove

This part describes how to arrange a centralized winding to achieve the highest efficiency. For fractional values q, two indivisible integers can be represented [27]:

$$q = \frac{b}{c} \tag{8}$$

As an example, we consider a combination that has 12 grooves and 14 poles.

$$q = \frac{12}{3 \times 14} = \frac{2}{7} \tag{9}$$

### F. DETERMINING THE EFFECT OF CENTRALIZED WINDING ON INCREASING FLUX ATTENUATION CAPABILITY IN SPM MOTOR

The SPM of motor is a very poor choice for wide access to high speeds under constant power. The main reason for this can be found in the SPM of motor characteristic flow, which is defined as follows:

$$I_{ch} = \frac{\Psi_m}{L_d} \tag{10}$$

In this regard, $\Psi_m$ is the effective value (rms) of the permanent magnet bond flux, and $L_d$ is the inductance of the d-axis (which is equal to the inductance of the q-axis in SPM). $I_{ch}$ defines the amount of current that, if applied along the d-axis, cancels out the entire permanent magnetic flux and a complete attenuation of the flux will occur. Therefore, the condition for attenuation of the optimal flux in PM motors occurs when the characteristic current is equal to the nominal current ($I_R = I_{ch}$) where IR is the nominal current of the electric motor.

### G. CONCENTRATED GROOVE-FRACTIONAL WINDING ARRANGEMENT ANALYSIS

In this section, a combination of 12 grooves and 10 poles is selected as a suitable combination for analysis. This compound is classified in the family q = 2.5. In this section, we analyze this combination. The reason for choosing this combination is:

1- Single layer winding can be used.
2- It has a high $k_{w1}$ equal to 0.966.
3- Ensures low torque cogging due to high LCM value (s, 2p).
4- Its radial forces are zero due to having an even value of *K*.

The single-layer centralized winding with SPP = 2.5 is compared with the conventional wide winding with SPP = 1. The analysis method is based on the winding function introduced in the reference [27]. The phase *A* winding arrangement of both designs is shown in Figure 4. It can be seen that there is a significant difference between the two designs. In a centralized winding with SPP = 2.5, for every 10 poles of the rotor, 2 windings of phase *A* are placed in four grooves. This winding is referred to as winding number 1. In comparison, a wide winding with 30 grooves and 10 poles (SPP = 1) has 5 windings laid in 10 grooves.

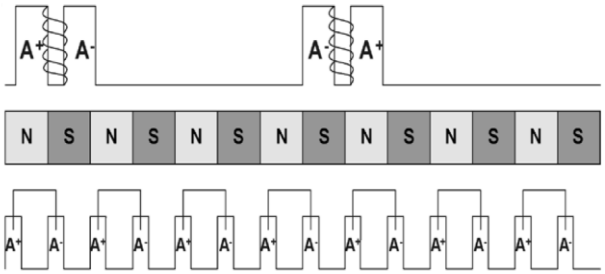


**FIGURE 4. Comparison between fractional groove concentrated winding (SPP = 2.5) and wide coil**

The constraint of the bond flux is the same. The first step is that both coils have a constant magnetic flux of equal magnitude. The centralized coil with SPP = 2.5 has N1 revolutions per coil and the wide coil with SPP = 1 has N2 revolutions per coil (All coils of each phase of the series are assumed). The permanent magnet bond flux is calculated as follows:

$$\Psi_a = r_g L_{eff} \int_0^{2\pi} N_a(\theta) B(\theta) d\theta \quad (weber.Turns) \tag{11}$$

Where $\Psi_a$ represents Phase A permanent magnet bond flux, $r_g$ is radius of air distance, $L_{eff}$ gives effective axial length of the electric motor, $N_a$ is Phase A winding function, θ represents the angle is around the air gap, B provides density of permanent magnetic flux in the air gap.

Since the synchronous component of the permanent magnet coupling flux is considered, only the principal component (first harmonic) of the B field is considered. It is assumed that both designs have the same rotor structure. Therefore, B is the same in both designs:

$$B_a = B_{max} \sin(p\theta) \qquad (Tesla) \tag{12}$$

$B_{max}$ is the maximum principal component of the constant magnetic flux density at air distance and P is the rotor pole pair number. For instance, for 12 grooves 10 poles we have:

$$\psi_1 = 2 r_g l_{eff} \int_{-\theta_1/2}^{\theta_1/2} N_1 B_{max} \sin(p\theta + 90^{\circ}) d\theta = r_g l_{eff} \times \frac{4}{\pi} k_{w1} N_1 B_{max} \tag{13}$$

Where $\theta_1$ is equal to π / 6 and $k_{w1}$ = 0/966 for q = SPP = 2.5. Also, for 30 grooves and 10 poles:

$$\psi_2 = 2 r_g l_{eff} \int_0^{\theta_2} \frac{N_2}{2} B_{max} \sin(p\theta) d\theta = r_g l_{eff} \times 2 k_{w2} N_2 B_{max} \tag{14}$$

Where $\theta_2$ is equal to π / 5 and $k_{w2}$ = 1 for q = SPP = 1

According to the statement, both coils must have the same synchronous component of the permanent magnet magnetic flux; therefore:

$$N_1 = \frac{p}{2 k_{w1}} N_2 = 2.6\, N_2 \tag{15}$$

This article has been accepted for publication in a future issue of this journal, but has not been fully edited. Content may change prior to final publication. Citation information: DOI 10.1109/ACCESS.2020.3041739, IEEE Access



Figure 5 shows the centralized winding function fraction groove 12 grooves 10 poles. Figure 6 also displays wide winding function 30 grooves 10 poles [28].

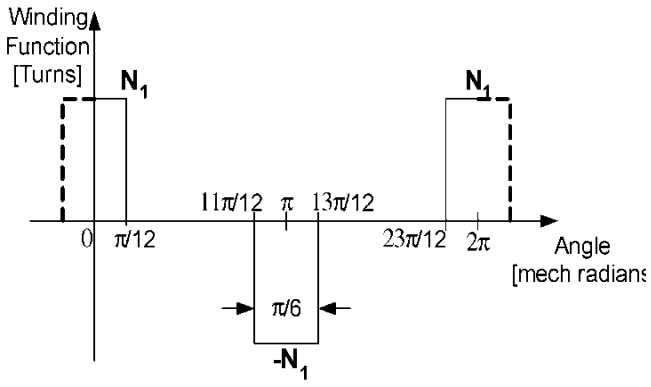


**FIGURE 5.** **Centralized winding function fraction groove 12 grooves 10 poles**

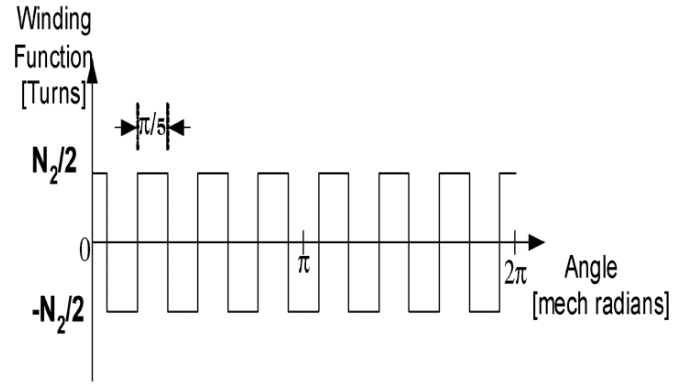


**FIGURE 6.** **Wide winding function 30 grooves 10 poles**

### *H. INDUCTION CALCULATIONS FOR SPM MOTOR*

Indoor and cross-phase inductance for the two windings mentioned in the previous section is calculated analytically in the SPM motor. For this purpose, we use the following two relations [26].

$$L_{aa} = \frac{\mu_0 r_g l_{eff}}{g} \int_0^{2\pi} N_a^2(\theta) d\theta \qquad (H) \qquad (16)$$

$$L_{ab} = \frac{\mu_0 r_g l_{eff}}{g} \int_0^{2\pi} N_a(\theta) N_b(\theta) d\theta \qquad (H) \qquad (17)$$

Where $L_{aa}$ is inductance insider phase *A*, $L_{ab}$ gives the cross-inductance between phase *A* and *B*; *g* provides air gap thickness. We need to define $L_d$ as an inductance of axis *d*, where $L_d = L_{aa} + L_{ab}$.

The inductances will be equal for both windings; for 12 grooves 10 poles with centralized groove - fraction:

$$L_{aa} = \frac{\mu_0 r_g l_{eff}}{g} N_1^2 \frac{\pi}{3} \qquad L_{ab} = L_{ac} = 0 \qquad (H) \qquad (18)$$

$$L_d = \frac{\mu_0 r_g l_{eff}}{g} N_1^2 \frac{\pi}{3} \qquad (H) \qquad (19)$$

For 30 grooves 10 poles is equal to:

$$L_{aa} = \frac{\mu_0 r_g l_{eff}}{g} N_2^2 \frac{\pi}{2} \qquad L_{ab} = \frac{L_{ac}}{3} \qquad (H) \qquad (20)$$

$$L_d = \frac{\mu_0 r_g l_{eff}}{g} N_2^2 \frac{2\pi}{3} \qquad (H) \qquad (21)$$

The ratio of inductances under the same bond flux conditions will be equal to:

$$\frac{L_{\substack{d \\ -conc}}}{L_{d-dis}} = \frac{N_1^2}{2N_2^2} = 3.38 \qquad (H) \qquad (22)$$

This is a very important result because it shows that for a fixed coupling flux, replacing the wide coil (SPP = 1) with the groove-fraction coil (SPP = 2.5) increases the inductance of the d-axis by more than three times. Give. As a result, the characteristic current of the electric motor (*Ich*) is reduced in the same proportion, and with a suitable design, the condition *IR*=*Ich* can be provided.

### *I. INDUCTANCE CALCULATIONS FOR INTERNAL PERMANENT MAGNET SYNCHRONOUS MOTOR*

One of the problems in the analysis of the internal permanent magnet synchronous motor that causes internal complexity is the saturation of iron in some parts of the rotor and stator and also the inequality of the inductance of the d and q axes. Therefore, providing an analytical analysis can be very useful.

In this paper, we carry out the finite element technique to calculate the inductance of the d and q axes. The calculation method is as follows. In this method, as in the permeabilization method, the effect of the magnet is removed without removing the magnetic driving force. Besides, the bond flux is calculated for two different working points close to each other. In order to eliminate the effect of the coupling flux of the q axis, when calculating the inductance of the d axis, we consider the q axis current constant. According to reference [27], inductance of axis's *d* and *q* can be given in equations (23) and (24), also details of the inductance calculation method is given in Figure 7.

$$L_d = \left(\frac{\varphi_{d1} - \varphi_{d2}}{I_{d1} - I_{d2}}\right)_{i_q = constant} \qquad (23)$$

$$L_q = \left(\frac{\varphi_{q1} - \varphi_{q2}}{I_{q1} - I_{q2}}\right)_{i_d = constant} \qquad (24)$$

This article has been accepted for publication in a future issue of this journal, but has not been fully edited. Content may change prior to final publication. Citation information: DOI 10.1109/ACCESS.2020.3041739, IEEE Access



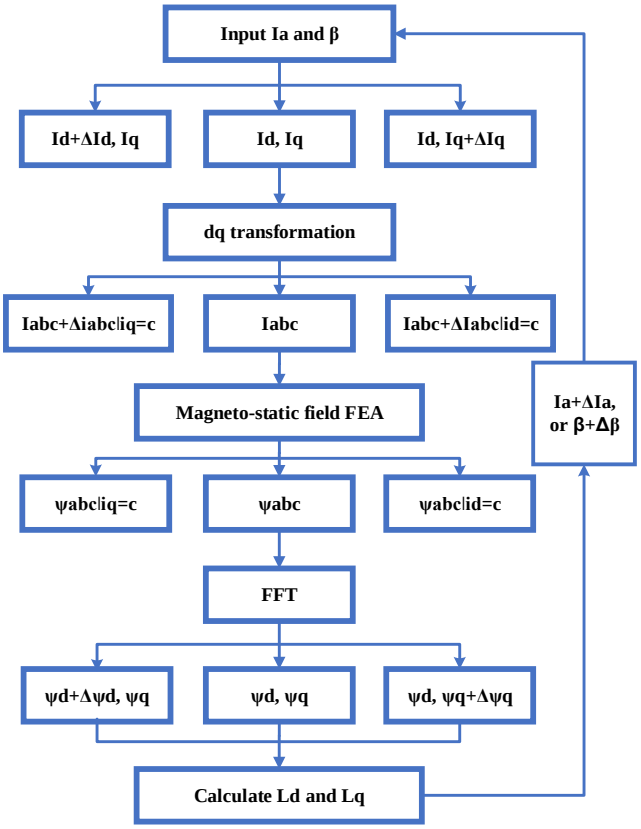


**FIGURE 7.** **Inductance calculation method** [27]

Then, by presenting a new design and using the sensitivity analysis method, the proposed design has been improved. In this method, by making a series of holes in the rotor surface, the toothed ripple torque is reduced and as a result, the torque rips. The variables considered in this design in the sensitivity analysis include the position and radius of each of the holes created. Using these holes, we were able to reduce the torque ripple in the proposed motor by more than 8% without reducing the average torque.

Toothed torque is caused by the reaction between the rotor poles and the internal gear structure of the stator and is independent of the stator current. To calculate the amount of energy stored in the air distance according to the position of the rotor, these pulses can be calculated as follows.

$$T_{cogging} = \frac{\partial W_{co}}{\partial \theta_r} = \frac{\partial}{\partial \theta_r}\left(\sum_{n=1}^{Q_s} W_n\right) \quad (25)$$

In any angular position of the rotor (θ), the total energy stored in the volume of the machine can be created by integrating the energy element per unit volume in the entire air space. This is done by integrating the magnetic flux density profile in the middle of the air gap, in the no-load mode of the electric motor $B_g(r,\theta)$, in a groove step *(Wr + Ws)* that includes the width of one tooth and one groove. It is acceptable. Finally, by calculating this integral numerically, the toothed ripple torque will generally be calculated as equation (26). The following equation is used to calculate the energy stored in air space.

$$W_n = r_g \int_0^L \int_{\theta_1}^{\theta_2} \int_0^g \frac{B_g^2}{2\mu_0} dg d\theta dl \quad (26)$$

Where $r_g$ is the radius of the air distance, $\theta_1$ and $\theta_2$ are the angle of one step of the groove, and $L$ is the length of the motor. As shown in the above equations, the flux density in the air gap is one of the most important factors in creating toothed torque. Based on these relationships, in case of decreasing the number of flux density harmonics and also increasing the first harmonic amplitude, the toothed torque can be reduced. To determine the position and number of holes created, we use the static state of the rotor and determine the flux density. Figure 8 shows the initial design by considering holes with a radius of one millimeter on the rotor surface. This initial design is then transformed into an improved design using the sensitivity analysis method.

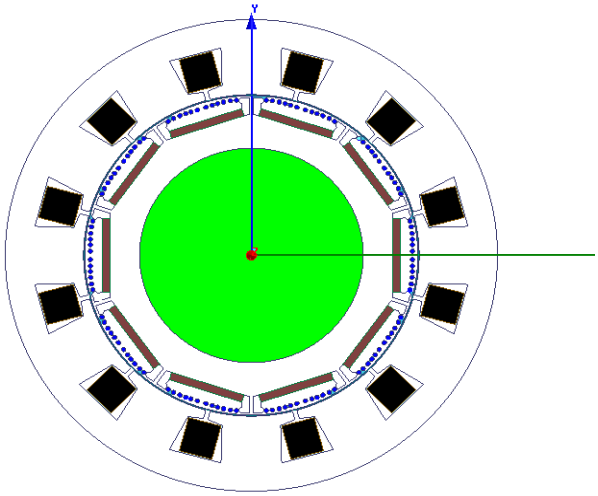


**FIGURE 8.** **Proposed motor with 12 holes per pole on the rotor surface**

## III. SIMULATION RESULTS

### *A. ANALYZING PROPOSED MOTOR WITH 12 HOLES PER POLE ON THE ROTOR SURFACE*

In order to achieve the optimal dimensions of the holes created, we use the sensitivity analysis method. For this purpose, we change each hole from the minimum radius (0.5 mm) to a radius of 1 mm, but the H6 hole will change to 1.6 mm; we also calculate the torque at the base speed (1100 rpm) for each of the modes to calculate the optimal hole radius.

Figure 9 shows the configuration of numbering the holes. The number of modes for each hole is three modes (0.5, 0.75 and 1 mm).

This article has been accepted for publication in a future issue of this journal, but has not been fully edited. Content may change prior to final publication. Citation information: DOI 10.1109/ACCESS.2020.3041739, IEEE Access



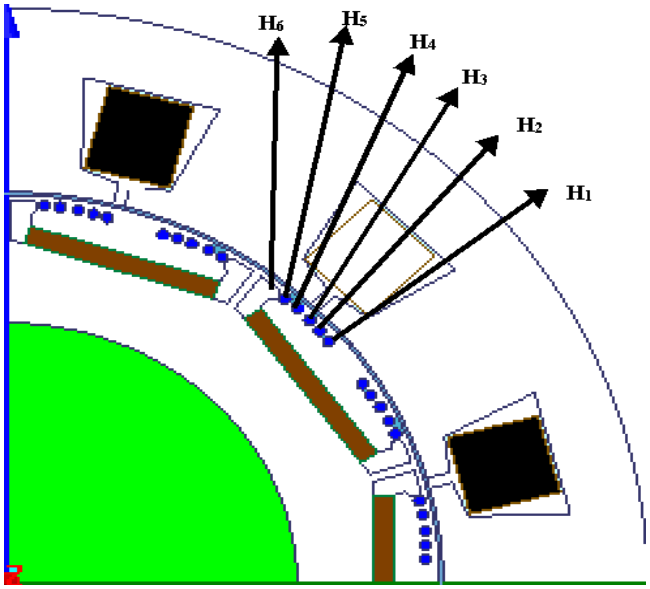


**FIGURE 9.** **The configuration of numbering the holes**

In the first step, to calculate an optimal dimension for all the holes, we change the radius of all the holes together from 0.5 to 1 mm and measure the torque at the base speed. An important factor to consider in this section is the torque ripple factor; this factor is given in Equation (27).

$$F = \left|\frac{T_{max} - T_{min}}{T_{avg}}\right| \times 100 \qquad (27)$$

In this equation, $T_{max}$ is the maximum value of the torque amplitude based on velocity. $T_{min}$ is the minimum value of the torque amplitude at the base velocity, and $T_{avg}$ is the mean value of the torque. The F function is a percentage and the main goal in this process is to minimize the value of $F$. The recovery process should be such that it keeps the value of $F$ to zero by keeping the average torque constant. Figure 10 shows the torque variation curve for radius changes of all holes from 0.5 mm to 1 mm.

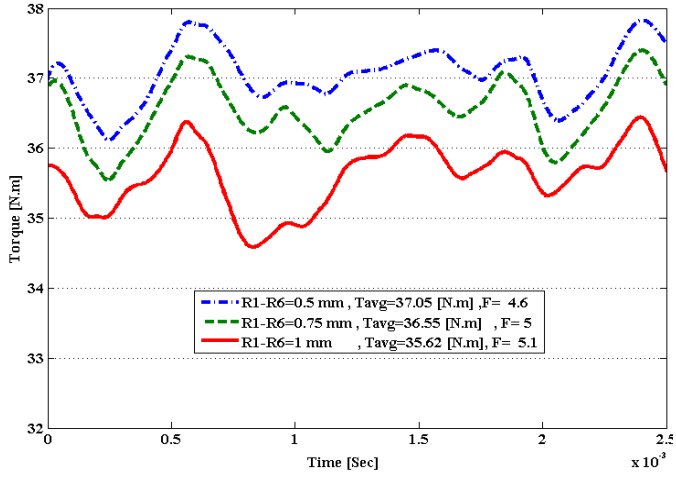


**FIGURE 10.** **Torque variation curve over time for hole radius changes**

As shown in Figure 10, the best mode has an average torque of 37 Nm and a ripple of 4.5%. Then, in order to obtain the optimal dimensions of each hole, we change its radius from 0.5 to 1 mm and calculate the two factors of average torque and $F$ to obtain the optimal dimension.

Figure 11 shows the torque variation curve over time for H1 hole radius changes. As shown in Figure 11 the best case is the same radius of 0.5 mm for H1. As a result, this radius remains constant at this value, and this value is considered the optimal value for this hole. Figure 12 also illustrates the torque change curve for H2 hole radius changes. As can be seen from the Figure 12, the torque decreases with increasing radius of the ripple hole, the average torque also decreases with decreasing torque ripple. Therefore, the best case is considered to be a radius of 0.75 mm. Figure 13 displays the time-varying torque change curve for H3 radius changes from 0.5 mm to 1 mm over time. As shown in this Figure and the data obtained, the best case is a radius of 0.5 mm. Figure 14 shows the torque change curve over time for H4 radius changes. As can be seen from this Figure, the best case for the R4 hole is a radius of 0.5 mm.

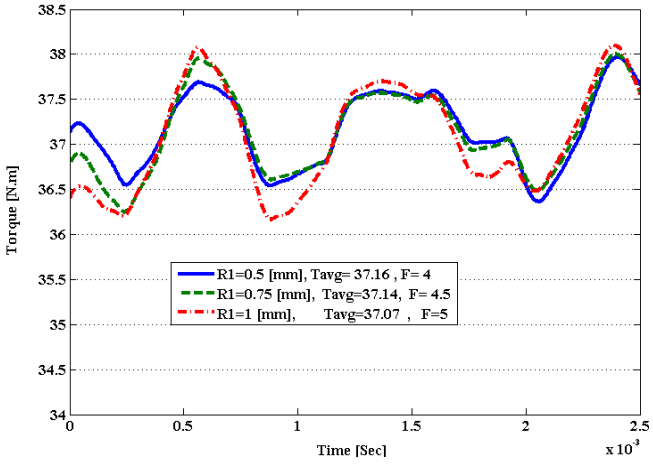


**FIGURE 11.** **Torque variation curve over time for R1 hole radius changes**

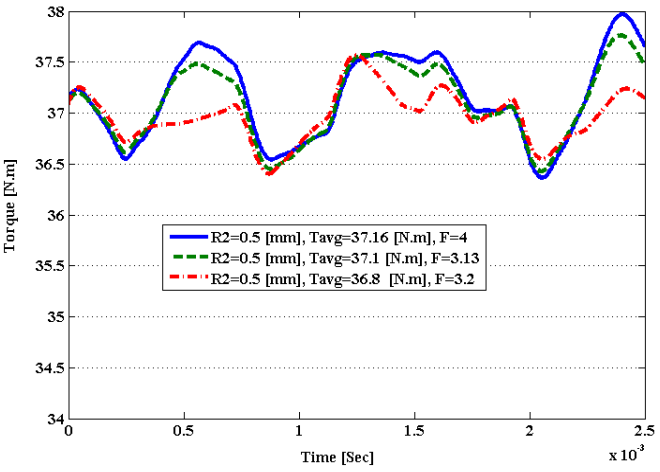


**FIGURE 12.** **Torque change curve for H2 hole radius changes**

This article has been accepted for publication in a future issue of this journal, but has not been fully edited. Content may change prior to final publication. Citation information: DOI 10.1109/ACCESS.2020.3041739, IEEE Access



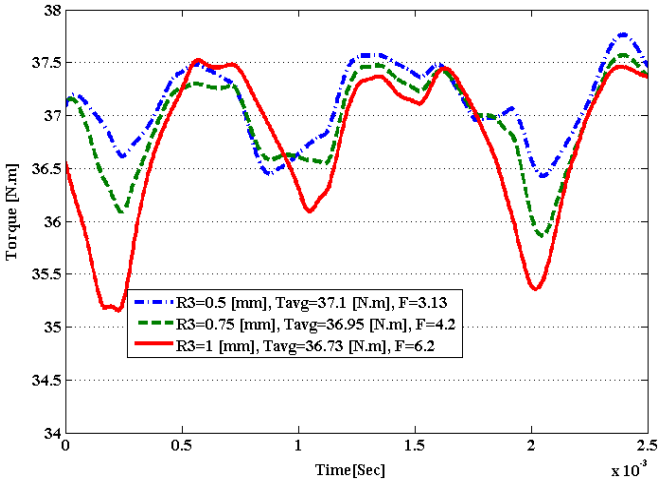


**FIGURE 13.** **Torque change curve over time for H3 radius changes**

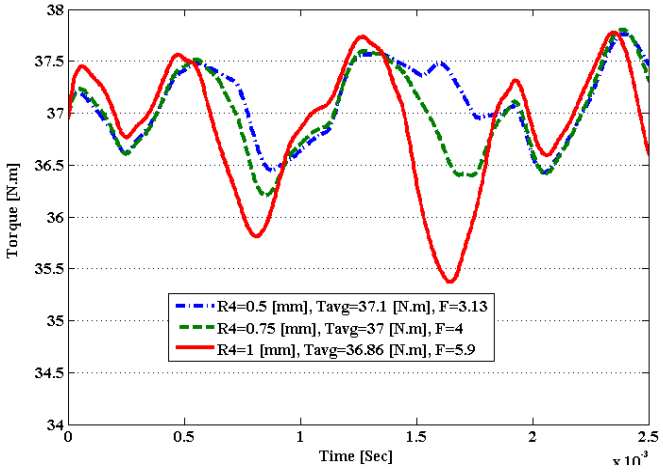


**FIGURE 14.** **Torque change curve over time for radius changes H4**

Figure 15 provides the change curve for H5. In this case, also, a radius of 0.5 mm is optimal.

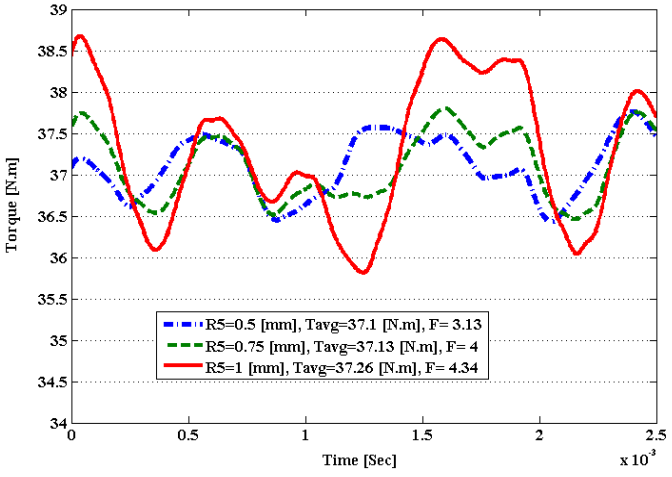


**FIGURE 15.** **Torque change curve over time for H5 radius changes**

Figure 16 shows the torque variation for H6 radius changes. Unlike other holes, the H6 radius varies from 0.5 mm to 1.6 mm. As shown in the Figure, the best radius for the H6 is 1.3 mm.

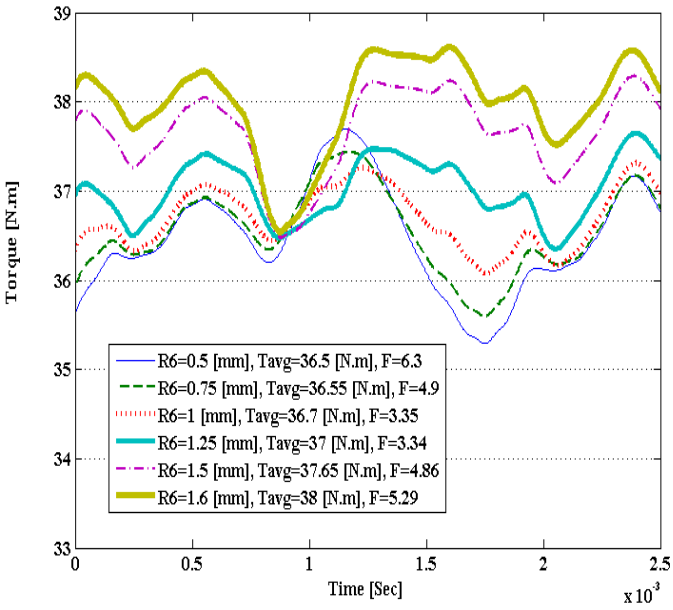


**FIGURE 16.** **Torque variation curve over time for H6 radius changes**

### *B. Dimensions and parameters of the proposed internal permanent magnet synchronous motor and wide winding structre*

Internal permanent magnet synchronous motor, 12 10-pole grooves, with single-layer centralized winding designed to attenuate improved flux. The proposed design electric motor is shown in Figure 17. The parameters of the proposed electric motor are also given in Table V. Figure 18 shows the flux lines for the proposed 12-pole 10-pole motor.

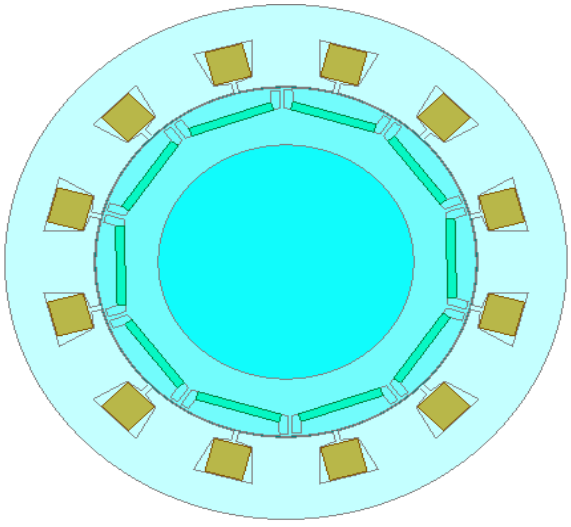

**FIGURE 17.** **Designed cross section of the motor**

This article has been accepted for publication in a future issue of this journal, but has not been fully edited. Content may change prior to final publication. Citation information: DOI 10.1109/ACCESS.2020.3041739, IEEE Access



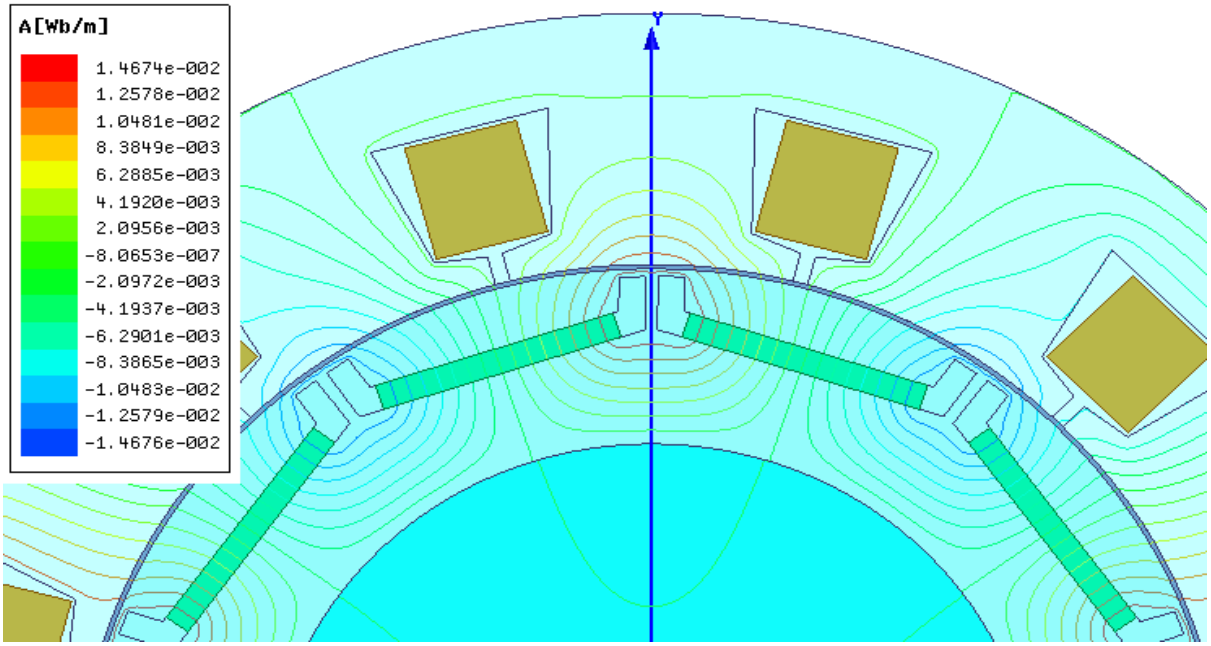


**FIGURE 18.** **Flux lines for the proposed 12-pole 10-pole motor**

TABLE V
RECOMMENDED ELECTRIC MOTOR PARAMETERS

| Parameters | Value | Parameters | Value |
|---|---|---|---|
| Number of grooves | 12 | Number of poles | 10 |
| Number of phases | 3 | Groove on the pole on the phase | 2/5 |
| Series number of rounds | 72 | Number of parallel routes | 1 |
| External radius of the rotor | 74.4 (mm) | Internal radius of the rotor | 50 (mm) |
| External radius of the stator | 110 (mm) | Internal radius of stator | 75 (mm) |
| Thickness of air gap | 0.6 (mm) | Permanent magnet thickness | 3.5 (mm) |
| The thickness of the iron bridge above the air-bridge | 1 (mm) | Effective electric motor length | 100 (mm) |
| Groove opening width ($w_o$) | 2 (mm) | The thickness of the iron behind the groove | 12 (mm) |
| Groove height | 17 (mm) | Top width of the groove | 23.9 (mm) |
| The width of the groove | 15.8 (mm) | Permanent magnet length | 34 (mm) |
| Permanent magnetic arc angle | 32 (degree) | Permanent magnetic residue | 1.5 (Tesla) |
| Nominal characteristic current (IR) | 17.38 (Arms) | Rated voltage | 110 (Vrms) |

Figure 19 displays the radial field created in the middle of the air gap for the proposed electric motor. Figure 20 shows the tangential field in the middle of the air gap for the propulsion electric motor.

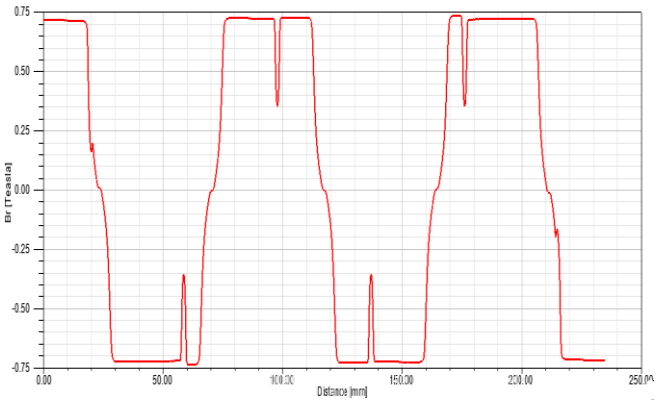


**FIGURE 19.** **Radial field at no load for the proposed motor**

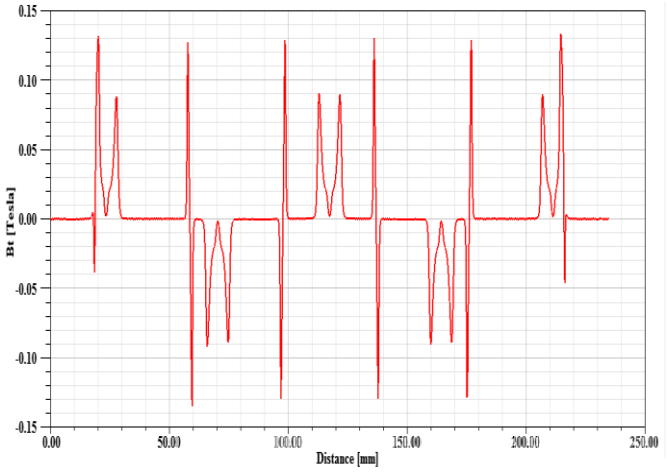


**FIGURE 20.** **Tangential field change curve for the proposed motor (SPP = 2.5)**

This article has been accepted for publication in a future issue of this journal, but has not been fully edited. Content may change prior to final publication. Citation information: DOI 10.1109/ACCESS.2020.3041739, IEEE Access



Figure 21 depicts the excitation voltage and its harmonic spectrum for the proposed motor. In order to validate the proposed method, the simulation results for the proposed motor (SPP = 2.5) and the motor with wide winding (SPP = 1) are compared. Figure 22 compares the ripple torque generated by these two motors.

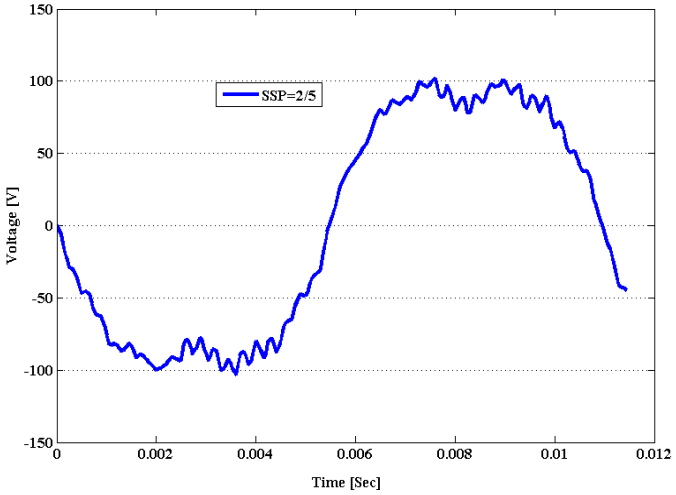


**FIGURE 21. Anti-drive voltage curve for motor with SPP = 2.5 and at nominal speed 1100 rpm**

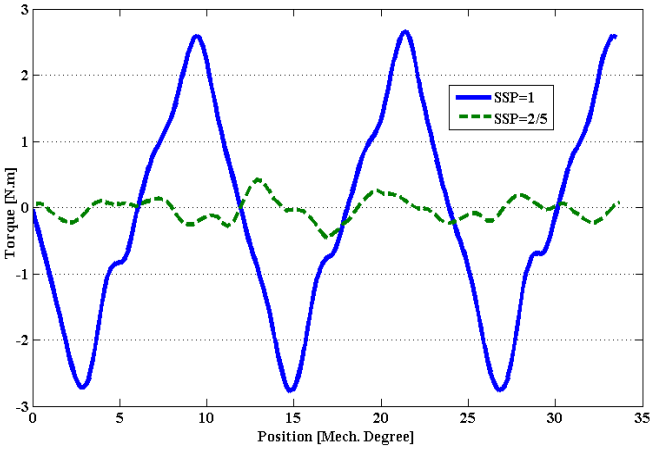


**FIGURE 22. Comparison of ripple torque for the proposed motor (SPP = 2.5) and motor with wide winding (SPP = 1)**

Torque ripple factor (TRF) is presented in equation (28). Given the equal amplitude of the current for both motors, the torque for both motors is shown in Figure 23 per maximum current. The average torque of these two motors is 37 Nm. The TRF is 11.1% for the proposed motor and 35.15% for the motor with wide winding.

$$\mathrm{TRF} = \frac{T_{pp}}{T_{av}} \times 100 \qquad (28)$$

Figure 24 displays the voltage variation curve at the base speed for the proposed motor and the wide-motor motor. The first harmonic of both curves is effective at 107 volts. As shown in the Figure 24, the input voltage due to the injection current is less harmonic for the wide-winding motor than for the centrally wound winding motor.

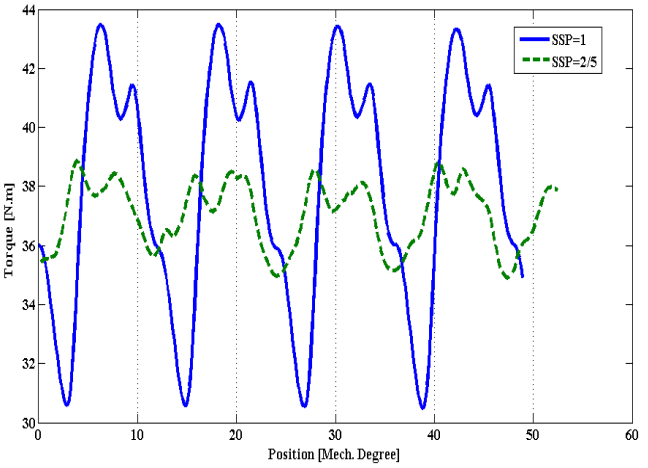


**FIGURE 23. Production torque for the proposed motor and the motor with wide winding**

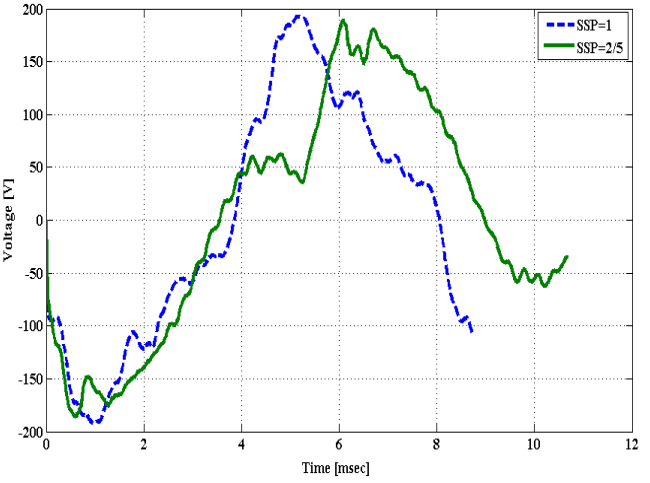


**FIGURE 24. Input output voltage change curve in both motors**

In order to compare the maximum output speed as well as the output power of the electric motor, we change the speed from zero to the maximum electric motor speed, and calculate the amount of power for each of the different modes. In order to calculate the power of the vector angle of the motor current on the maximum circle of the motor current, we change it from 90 degrees to 180 degrees. Figure 25 presents the power change curve in terms of speed for the proposed motor. Figure 26 also depicts the output power change curve in terms of speed for the motor with SPP = 1. From Figures 25 and 26, which are power curves in terms of speed, it can be concluded that the motor with centralized winding has better flux attenuation conditions. Figure 27 illustrates the meshing (wiring) configuration for performing the finite element analysis process for the proposed electric motor. Besides, torque and terminal voltage curve produced by the proposed motor at a speed of 12000 rpm are depicted in the Figure 28 and Figure 29 respectively.

This article has been accepted for publication in a future issue of this journal, but has not been fully edited. Content may change prior to final publication. Citation information: DOI 10.1109/ACCESS.2020.3041739, IEEE Access



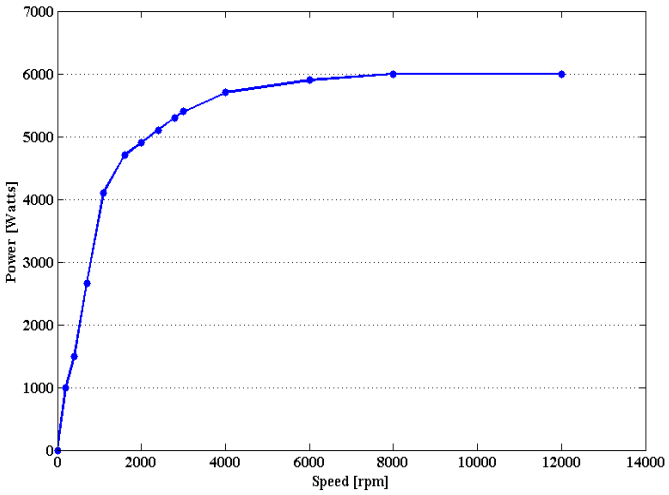


FIGURE 25. Power change velocity curve for the proposed motor

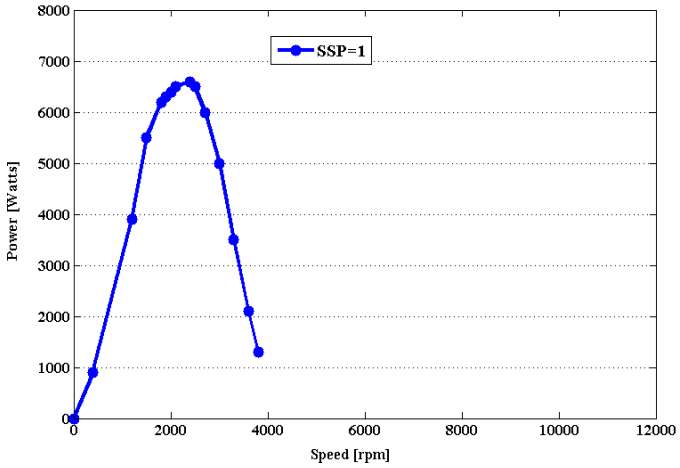


FIGURE 26. Output power change curve in terms of speed for motor with SPP = 1

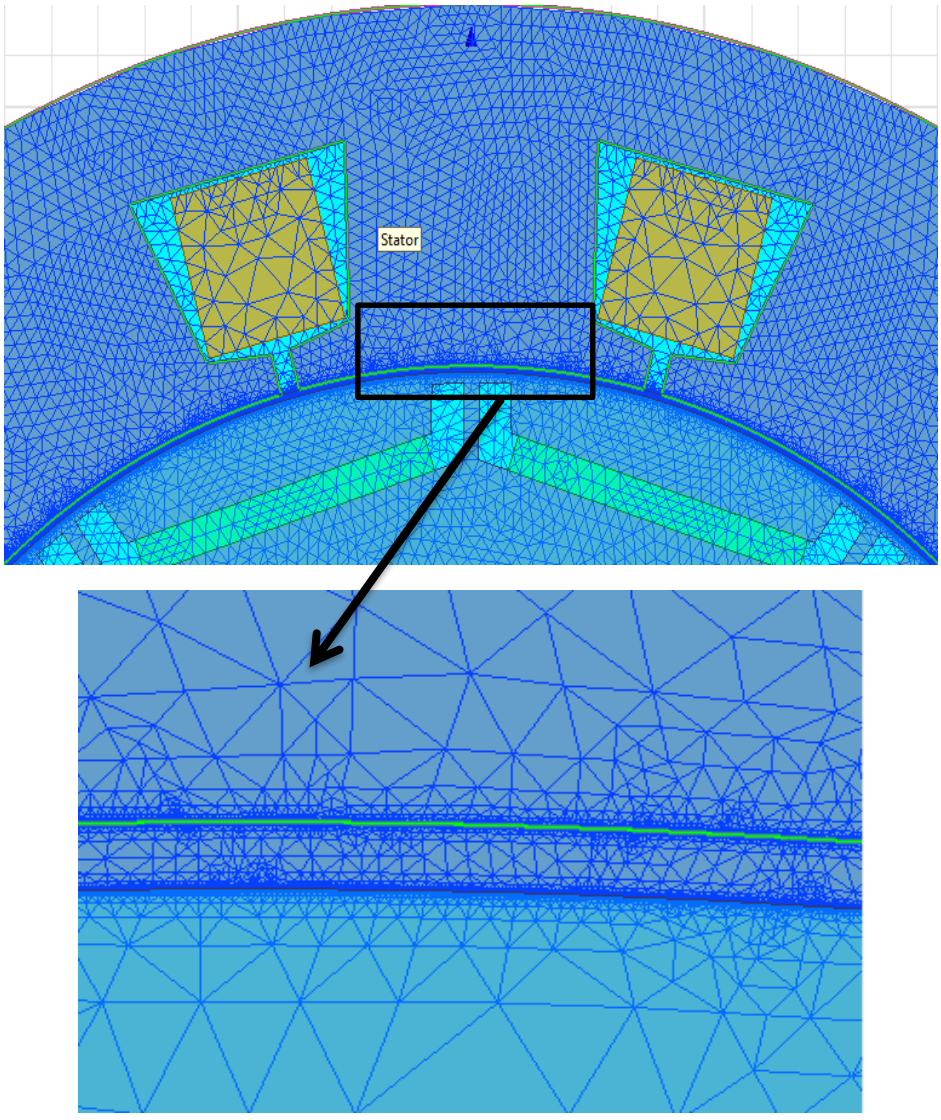


FIGURE 27. Wiring configuration for performing the finite element analysis process for the proposed electric motor

This article has been accepted for publication in a future issue of this journal, but has not been fully edited. Content may change prior to final publication. Citation information: DOI 10.1109/ACCESS.2020.3041739, IEEE Access



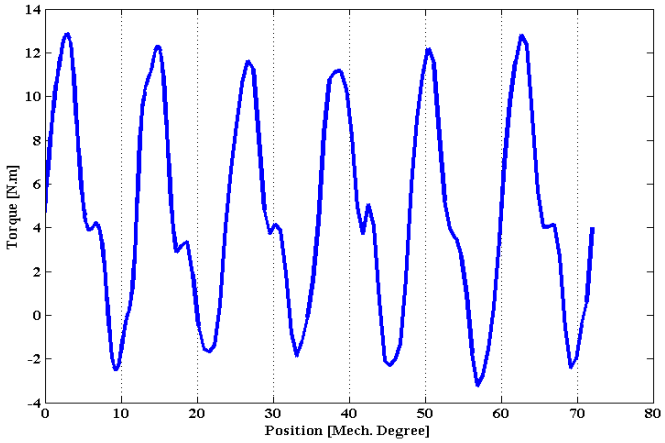


**FIGURE 28.** **Torque produced by the proposed motor at a speed of 12000**

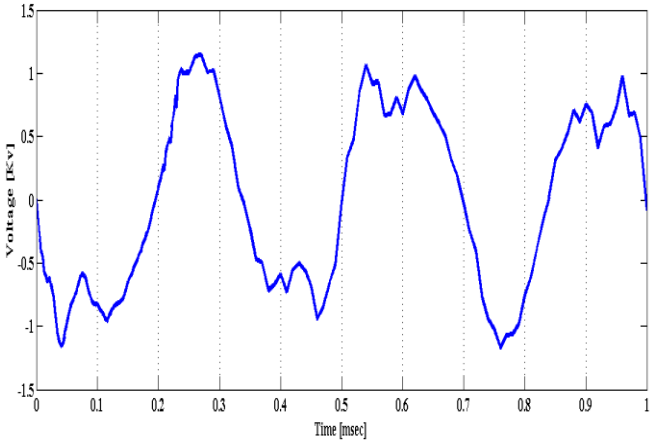


**FIGURE 29.** **Terminal voltage curve at 12000 rpm for the proposed motor**

The D and Q axis inductances for the proposed motor are shown in Figures 30 and 31, respectively.

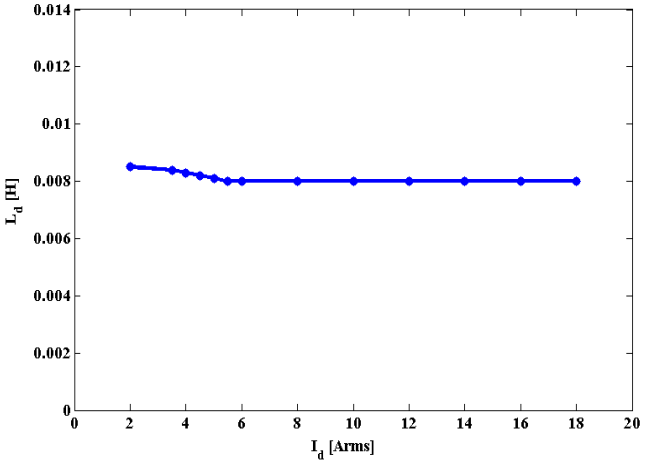


**FIGURE 30.** ***D*-axis inductance change curve in terms of current**

Figure 32 also presents the magnet of a permanent magnet for maximum velocity and two adjacent poles. As shown in this Figure, neither of the two adjacent poles has lost its magnetic property, and as a result, there is no problem with the permanent magnet of the motor, even in the worst conditions.

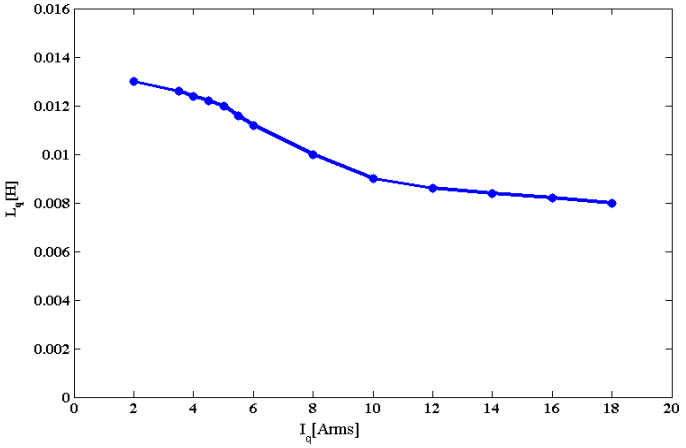


**FIGURE 31.** ***Q*-axis inductance change curve in terms of Q-axis current changes**

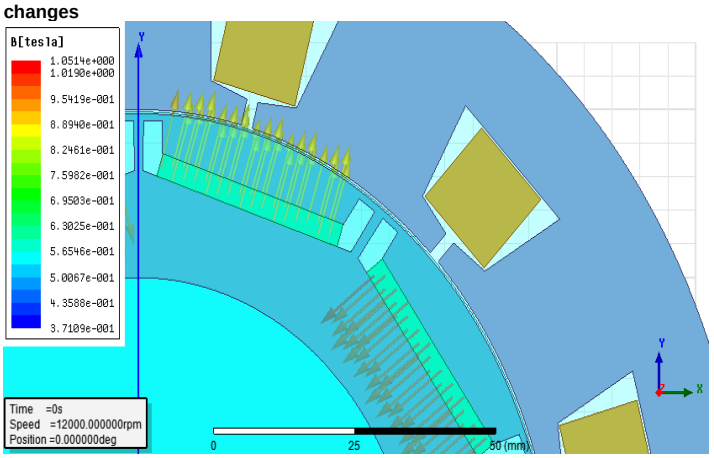


**FIGURE 32.** **Permanent magnetic residual vector at maximum speed**

### *C. Harmonic analysis*

In order to determine the number of holes created on the surface of the rotor, we use the study of the flux density harmonics in the air distance. By reducing the number of holes created, we examine two important factors to create the best case to reduce torque ripple without reducing the average torque. Here, the first factor can be the first harmonic amplitude. The higher the amplitude of the first harmonic, the higher the bonding flux will have more torque and power. The second factor is the amplitude of other harmonics compared to the first harmonic or total harmonic distortion (THD); as this factor decreases, the shape of the flux density gets closer to the sine, and as a result, the toothed torque decreases. To reduce the number of holes created on the rotor surface, we reduce the number of holes on the D-axis in pairs to achieve high first harmonic amplitude and a low THD. Figures 33 and 34 show the flux density and harmonic spectrum of the proposed motor in the state without creating a hole on the rotor surface, respectively.

This article has been accepted for publication in a future issue of this journal, but has not been fully edited. Content may change prior to final publication. Citation information: DOI 10.1109/ACCESS.2020.3041739, IEEE Access



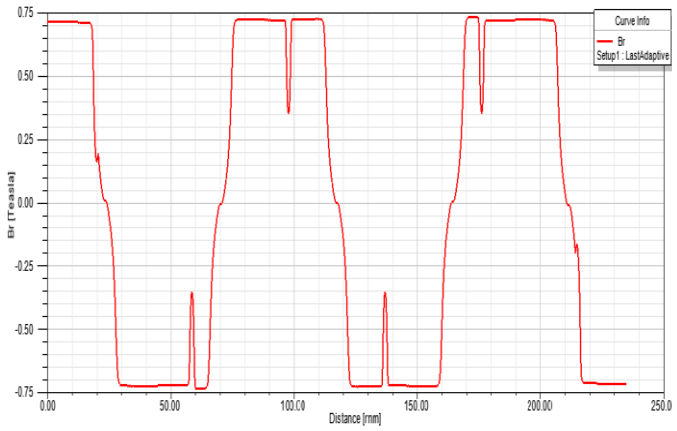


**FIGURE 33.** Flux density in the middle of the air gap in the hole-less state

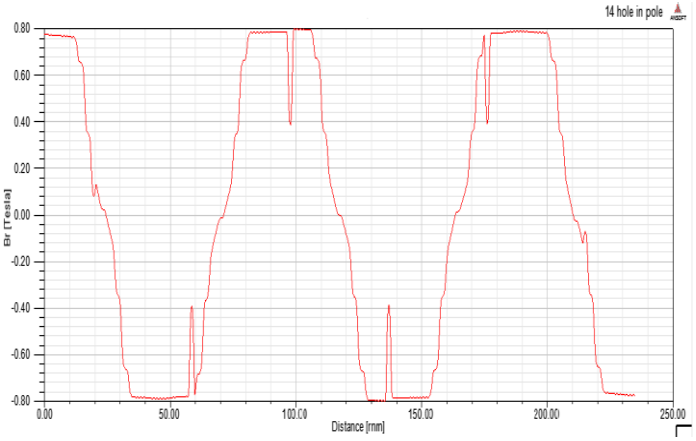


**FIGURE 35.** Flux density when there are 14 grooves on the surface of each pole

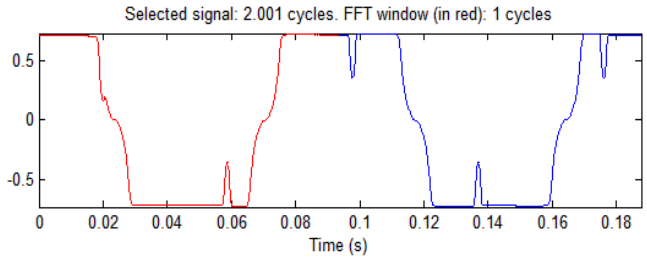


```
Sampling time     = 0.0001 s
Samples per cycle = 938
DC component      = 0.002116
Fundamental       = 0.8755 peak (0.6191 rms)

Total Harmonic Distortion (THD) = 28.08%

Maximum harmonic frequency
 used for THD calculation  = 4978.68 Hz (467th harmonic)

      0 Hz   (DC):          0.24%     90.0°
 10.661 Hz   (Fnd):       100.00%     90.7°
 21.322 Hz   (h2):          0.88%     32.4°
31.9829 Hz   (h3):         23.90%    267.1°
42.6439 Hz   (h4):          1.58%    -66.0°
53.3049 Hz   (h5):          7.06%     81.6°
63.9659 Hz   (h6):          1.87%    189.8°
74.6269 Hz   (h7):          1.76%     65.5°
85.2878 Hz   (h8):          1.83%     83.2°
95.9488 Hz   (h9):          6.92%    265.1°
 106.61 Hz (h10):          1.39%    -23.0°
117.271 Hz (h11):          7.14%    100.9°
127.932 Hz (h12):          0.80%    254.5°
```

**FIGURE 34.** Harmonic spectra and THD flux density in the hole-less state

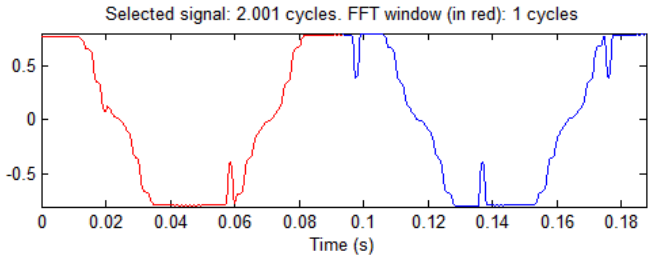


```
Sampling time     = 0.0001 s
Samples per cycle = 938
DC component      = 0.002029
Fundamental       = 0.8856 peak (0.6262 rms)

Total Harmonic Distortion (THD) = 15.28%

Maximum harmonic frequency
 used for THD calculation  = 4978.68 Hz (467th harmoni

      0 Hz   (DC):          0.23%     90.0°
 10.661 Hz   (Fnd):       100.00%     90.2°
 21.322 Hz   (h2):          0.71%     -1.4°
31.9829 Hz   (h3):          9.64%    258.4°
42.6439 Hz   (h4):          1.19%    -78.1°
53.3049 Hz   (h5):          6.25%    -80.2°
63.9659 Hz   (h6):          1.59%    194.2°
74.6269 Hz   (h7):          6.27%     82.1°
85.2878 Hz   (h8):          1.63%     91.4°
95.9488 Hz   (h9):          3.53%    258.3°
 106.61 Hz (h10):          1.31%     -9.3°
117.271 Hz (h11):          1.52%    151.2°
```

**FIGURE 36.** Harmonic spectrum for 14-hole mode

Figures 35 and 36 provide the flux density and harmonic spectrum for the proposed motor state with one millimeter holes on the entire surface of the rotor. In this case, each pole has 14 holes on the rotor surface.

Figures 37 and 38 illustrate the flux density and harmonic spectrum for the proposed motor with 12 holes at each pole, respectively.

Figures 39 and 40 depict the flux density and harmonic spectrum for the proposed motor with 10 holes per pole on the rotor. The harmonic voltage values for the proposed motor at 12,000 rpm are shown in Figure 41.

This article has been accepted for publication in a future issue of this journal, but has not been fully edited. Content may change prior to final publication. Citation information: DOI 10.1109/ACCESS.2020.3041739, IEEE Access



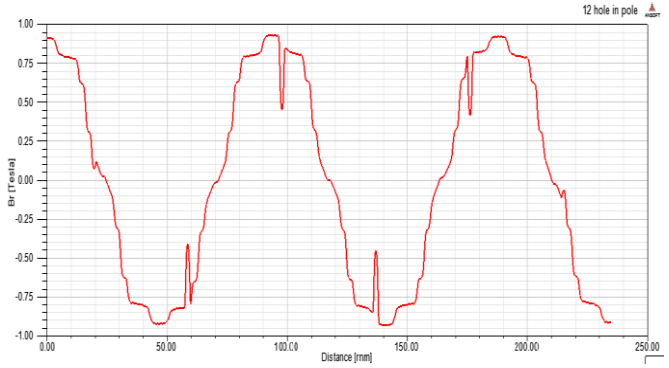


**FIGURE 37.** Flux density in the middle of the air gap in the case of 12 holes at each pole

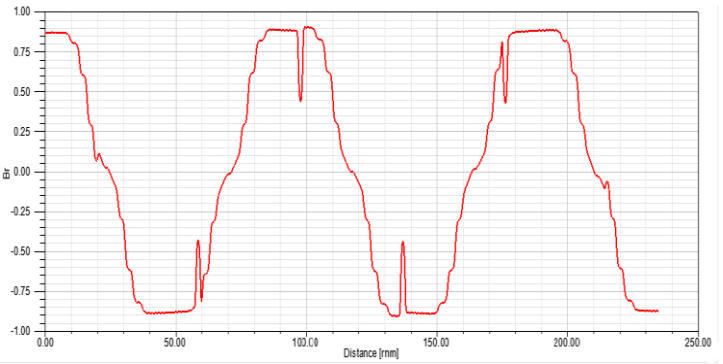


**FIGURE 39.** Flux density with 10 holes per pole

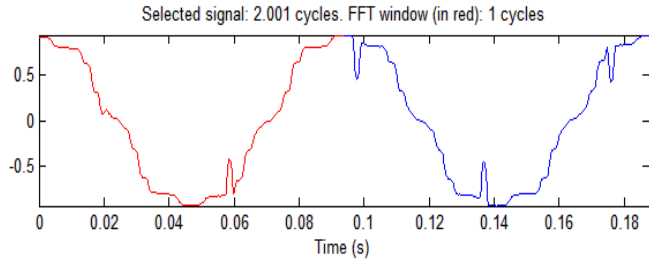


```
Sampling time     = 0.0001 s
Samples per cycle = 938
DC component      = 0.001546
Fundamental       = 0.9386 peak (0.6637 rms)

Total Harmonic Distortion (THD) = 11.48%

Maximum harmonic frequency
 used for THD calculation  = 4978.68 Hz (467th harmonic)

      0 Hz   (DC):          0.16%     90.0°
 10.661 Hz   (Fnd):       100.00%     90.0°
 21.322 Hz   (h2):          0.25%      7.3°
31.9829 Hz   (h3):          3.06%    245.6°
42.6439 Hz   (h4):          0.82%    -85.2°
53.3049 Hz   (h5):          4.65%    -76.3°
63.9659 Hz   (h6):          1.38%    186.9°
74.6269 Hz   (h7):          7.33%     85.6°
85.2878 Hz   (h8):          1.59%     88.8°
95.9488 Hz   (h9):          1.75%    244.7°
 106.61 Hz  (h10):          1.27%     -7.9°
```

**FIGURE 38.** Harmonic spectrum of charge density in the state of 12 holes per pole

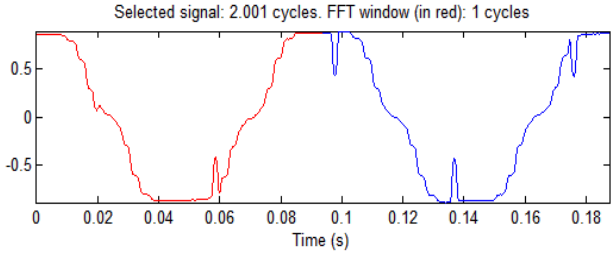


```
Sampling time     = 0.0001 s
Samples per cycle = 938
DC component      = 0.002501
Fundamental       = 0.9581 peak (0.6775 rms)

Total Harmonic Distortion (THD) = 12.32%

Maximum harmonic frequency
 used for THD calculation  = 4978.68 Hz (467th harmonic)

      0 Hz   (DC):          0.26%     90.0°
 10.661 Hz   (Fnd):       100.00%     90.1°
 21.322 Hz   (h2):          0.52%     16.4°
31.9829 Hz   (h3):          3.64%    240.2°
42.6439 Hz   (h4):          0.96%    -71.3°
53.3049 Hz   (h5):          8.48%    -84.8°
63.9659 Hz   (h6):          1.36%    199.5°
74.6269 Hz   (h7):          4.43%     82.0°
85.2878 Hz   (h8):          1.40%     92.9°
95.9488 Hz   (h9):          2.18%    256.4°
 106.61 Hz  (h10):          1.17%     -8.9°
117.271 Hz  (h11):          1.25%    154.4°
127.932 Hz  (h12):          0.97%    263.7°
138.593 Hz  (h13):          1.66%     56.0°
```

**FIGURE 40.** Harmonic spectrum of flux density in the case of 10 holes on the rotor surface

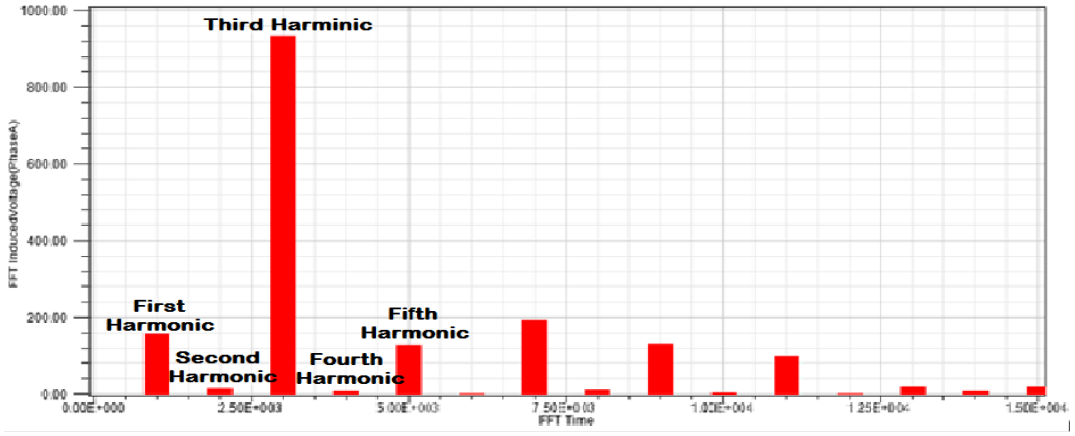


**FIGURE 41.** harmonic voltage values for the proposed motor at 12,000 rpm

As can be seen from these Figures, placing the rabid hole on the rotor surface increases the first harmonic amplitude and also decreases the THD drastically. In order to achieve a more efficient design, the number of holes created has been reduced. As can be seen from the obtained results, the best condition of the motor is with 12 holes per pole on the rotor surface. Because THD increases with decreasing number of holes and this increase in THD will increase the toothed torque range.

## IV. CONCLUSION

In this paper, the effect of wide and concentrated winding types on toothed ripple torque in internal permanent magnet motor has been investigated. By making holes in the rotor surface and by using the sensitivity analysis method, the structure of the internal permanent magnet electric motor was improved in order to reduce the toothed ripple torque and increase the average torque. In this method, the number, dimensions and location of holes were optimized using the sensitivity analysis method, which reduces the ripple toothed torque of the motor using two structures. In this regards, the electric motor torque was reduced to two suitable structures. By using a centralized coil instead of a wide coil, the toothed ripple torque has been reduced by approximately 75% while maintaining the average torque value. Also, by making holes in the rotor surface and optimizing it using the finite element method and open sensitivity analysis, the amount of ripple torque was reduced by 20%. Using the proposed method and using a concentrated winding instead of a wide winding, in addition to reducing spatial harmonics, the average torque value was also improved.

## REFERENCES

[1] X. Sun, Z. Shi, G. Lei, Y. Guo, and J. Zhu, "Analysis and design optimization of a permanent magnet synchronous motor for a campus patrol electric vehicle," *IEEE Transactions on Vehicular Technology*, vol. 68, pp. 10535-10544, 2019.

[2] N. d. A. B. Weber, B. P. da Rocha, P. S. Schneider, L. C. Daemme, and R. d. A. P. Neto, "Energy and emission impacts of liquid fueled engines compared to electric motors for small size motorcycles based on the Brazilian scenario," *Energy*, vol. 168, pp. 70-79, 2019.

[3] A. Nordelöf, E. Grunditz, S. Lundmark, A.-M. Tillman, M. Alatalo, and T. Thiringer, "Life cycle assessment of permanent magnet electric traction motors," *Transportation Research Part D: Transport and Environment*, vol. 67, pp. 263-274, 2019.

[4] J. Zhao, J. Wang, L. Zhou, W. Huang, Y. Ma, and Z. Zhang, "Cogging torque reduction by stepped slot-opening shift for interior permanent magnet motors," in *2019 22nd International Conference on Electrical Machines and Systems (ICEMS)*, 2019, pp. 1-4.

[5] P. Dini and S. Saponara, "Cogging torque reduction in brushless motors by a nonlinear control technique," *Energies*, vol. 12, p. 2224, 2019.

[6] Y. Ueda and H. Takahashi, "Cogging torque reduction on transverse-flux motor with multilevel skew configuration of toothed cores," *IEEE Transactions on Magnetics*, vol. 55, pp. 1-5, 2019.

[7] Y. Ueda and H. Takahashi, "Transverse-flux motor design with skewed and unequally distributed armature cores for reducing cogging torque," *IEEE Transactions on Magnetics*, vol. 53, pp. 1-5, 2017.

[8] J. G. Washington, G. J. Atkinson, and N. J. Baker, "Reduction of cogging torque and EMF harmonics in modulated pole machines," *IEEE Transactions on Energy Conversion*, vol. 31, pp. 759-768, 2016.

[9] T. Husain, I. Hasan, Y. Sozer, I. Husain, and E. Muljadi, "Cogging torque minimization in transverse flux machines," *IEEE Transactions on Industry Applications*, vol. 55, pp. 385-397, 2018.

[10] D. Xu, X. Jiang, Y. Tu, N. Li, and Q. Li, "Investigation of cogging torque reduction for a 6/10 hybrid axial field flux-switching permanent magnet machine by harmonic field current injection," *IET Electric Power Applications*, 2020.

[11] X. Zhu, D. Fan, Z. Xiang, L. Quan, W. Hua, and M. Cheng, "Systematic multi-level optimization design and dynamic control of less-rare-earth hybrid permanent magnet motor for all-climatic electric vehicles," *Applied Energy*, vol. 253, p. 113549, 2019.

[12] T. A. Huynh and M.-F. Hsieh, "Performance analysis of permanent magnet motors for electric vehicles (EV) traction considering driving cycles," *Energies*, vol. 11, p. 1385, 2018.

[13] Y. Yang, S. M. Castano, R. Yang, M. Kasprzak, B. Bilgin, A. Sathyan, *et al.*, "Design and comparison of interior permanent magnet motor topologies for traction applications," *IEEE transactions on transportation Electrification*, vol. 3, pp. 86-97, 2016.

[14] J.-H. Lee, D.-H. Kim, and I.-H. Park, "Minimization of higher back-EMF harmonics in permanent magnet motor using shape design sensitivity with B-spline parameterization," *IEEE Transactions on Magnetics*, vol. 39, pp. 1269-1272, 2003.

[15] D.-H. Kim, I.-H. Park, J.-H. Lee, and C.-E. Kim, "Optimal shape design of iron core to reduce cogging torque of IPM motor," *IEEE transactions on magnetics*, vol. 39, pp. 1456-1459, 2003.

[16] M. Jafari and S. A. Taher, "Thermal survey of core losses in permanent magnet micro-motor," *Energy*, vol. 123, pp. 579-584, 2017.

[17] O. Atlam and M. Kolhe, "Performance evaluation of directly photovoltaic powered DC PM (direct current permanent magnet) motor–propeller thrust system," *Energy*, vol. 57, pp. 692-698, 2013.

[18] H. addin Yousefian and H. M. Kelk, "A unique optimized double-stator permanent-magnet synchronous generator in high-power wind plants," *Energy*, vol. 143, pp. 973-979, 2018.

[19] H. Pairo, M. H. Khanzade, and A. Shoulaie, "Loss-based investigation and hybrid compensation of parameter variation effects on control of permanent magnet synchronous motors," *International Transactions on Electrical Energy Systems*, vol. 28, p. e2475, 2018.

[20] E. Kusuma and V. K. Thippiripati, "Effective predictive torque control scheme for four-level open-end winding permanent magnet synchronous motor drive," *International Transactions on Electrical Energy Systems*, p. e12536, 2020.

[21] T. Chen, P. Chen, J. Liang, S. Li, and B. Fahimi, "Maximum Torque Per Ampere Control of Interior Permanent Magnet Synchronous Motor via Optimal Current Excitation," in *2019 IEEE Energy Conversion Congress and Exposition (ECCE)*, 2019, pp. 7043-7048.

[22] G.-H. Kang, Y.-D. Son, G.-T. Kim, and J. Hur, "A novel cogging torque reduction method for interior-type permanent-magnet motor," *IEEE Transactions on Industry Applications*, vol. 45, pp. 161-167, 2009.

[23] R. Cao, C. Mi, and M. Cheng, "Quantitative comparison of flux-switching permanent-magnet motors with interior permanent magnet motor for EV, HEV, and PHEV applications," *IEEE Transactions on magnetics*, vol. 48, pp. 2374-2384, 2012.

[24] D. Dorrell, M. Popescu, L. Evans, D. Staton, and A. Knight, "Modern electrical machine analysis and design techniques applied to hybrid vehicle drive machines," in *2010 IEEE International Symposium on Industrial Electronics*, 2010, pp. 3728-3733.

[25] M. R. Shah and A. M. El-Refaie, "Eddy-current loss minimization in conducting sleeves of surface PM machine rotors with fractional-slot concentrated armature windings by optimal axial segmentation and copper cladding," *IEEE Transactions on Industry Applications*, vol. 45, pp. 720-728, 2009.

[26] E. Fornasiero, L. Alberti, N. Bianchi, and S. Bolognani, "Considerations on selecting fractional-slot nonoverlapped coil windings," *IEEE Transactions on Industry Applications*, vol. 49, pp. 1316-1324, 2013.

[27] A. M. El-Refaie, T. M. Jahns, and D. W. Novotny, "Analysis of surface permanent magnet machines with fractional-slot concentrated windings," *IEEE Transactions on Energy conversion*, vol. 21, pp. 34-43, 2006.

[28] M. S. Islam, R. Islam, T. Sebastian, A. Chandy, and S. A. Ozsoylu, "Cogging torque minimization in PM motors using robust design approach," *IEEE Transactions on Industry applications*, vol. 47, pp. 1661-1669, 2011.

**ALIREZA RAMEZANI** was born in Shiraz, Iran in 1984. He received B.S. degree in Electrical Engineering from Yazd Branch, Islamic Azad University and M.S. degree in Electrical Engineering from Jahrom Branch, Islamic Azad University, in 2010 and 2017, respectively. He is currently working for Fars Regional Electricity Company in Iran. His current research interests include operation, management and analysis of smart grids, distributed generation and electric machines.

**MOHAMMAD GHIASI** (Graduate Student Member, IEEE) is currently a research assistant at the Shiraz University of Technology, Shiraz, Iran. He received his B.S. degree in 2012 and M.S. degree in 2016, both in electrical power engineering. Since 2007 he has been with the Power Control Center (PCC) of Tehran Metro as a senior control power engineer. He is a member of the Tehran Construction Engineering Organization (TCEO). He is also the reviewer for several IEEE, IET, Elsevier, Springer, Wiley, Taylor & Francis and Sage journals and conferences. His research on modeling, simulation and optimization of power systems, integration and control of hybrid and distributed renewable energy resources, smart grids, as well as resilience and cyber security in power systems has led to multiple publications in these fields. He has 2 Hot Papers and 1 Highly-Cited paper, based on SciVal and Web of Science statistics.

**MOSLEM DEHGHANI** was born in Shiraz, Iran, in 1990. He received B.S. and M.S. degrees in Electrical Engineering from Islamic Azad University - Kazerun branch respectively in 2012 and 2014, and he started studying in Ph.D. degree in Electrical Engineering in 2019 at Shiraz University of Technology, Shiraz, Iran. His current research interests include power electronic, control, and cyber security analysis of smart grids, microgrid, smart city, HVDC systems as well as protection of power systems, fuzzy logic and signal processing

**TAHER NIKNAM.** (Member, IEEE) was born in Shiraz, Iran. He received the B.S. degree from Shiraz University, Shiraz, Iran, in 1998, and the M.S. and Ph.D. degrees from the Sharif University of Technology, Tehran, Iran, in 2000 and 2005, respectively, all in power electrical engineering. He is a faculty member with the Electrical Engineering Department, Shiraz University of Technology. His research interests include power system restructuring, impact of distributed generations on power systems, optimization methods, and evolutionary algorithms.

**PIERLUIGI SIANO** (M'09–SM'14) received the M.Sc. degree in Electronic Engineering and the Ph.D. degree in Information and Electrical Engineering from the University of Salerno, Fisciano, Italy, in 2001 and 2006, respectively. He is an Associate Professor with accreditation for Full Professor of Electrical Energy Engineering with the Department of Industrial Engineering, University of Salerno. His research interests include demand response, integration of distributed energy resources in smart grids and planning, and management of power systems.

**Hassan Haes Alhelou** (Senior Member, IEEE) is a faculty member at Tisheen University, Lattakia, Syria.
He is included in the 2018 and 2019 Publons list of the top 1% best reviewer and researchers in the field of engineering. He was the recipient of the Outstanding Reviewer Award from Energy Conversion and Management Journal in 2016, ISA Transactions Journal in 2018, Applied Energy Journal in 2019, and many other Awards. He was the recipient of the best young researcher in the Arab Student Forum Creative among 61 researchers from 16 countries at Alexandria University, Egypt, 2011. He has published more than 100 research papers in the high quality peer-reviewed journals and international conferences. He has also performed more than 500 reviews for high prestigious journals including IEEE Transactions on Industrial Informatics, IEEE Transactions on Industrial Electronics, Energy Conversion and Management, Applied Energy, International Journal of Electrical Power & Energy Systems. He has participated in more than 15 industrial projects. His major research interests are Power systems, Power system dynamics, Power system operation and control, Dynamic state estimation, Frequency control, Smart grids, Micro-grids, Demand response, Load shedding, and Power system protection.